

On the linear finite element analysis of fully-coupled point contact elastohydrodynamic lubrication problems

Sarfraz Ahmed^{*1}, Christopher E. Goodyer², and Peter K. Jimack³

^{1,2,3}*School of Computing, University of Leeds, UK*

Abstract

The fully coupled approach for the solution of elastohydrodynamic lubrication (EHL) point contact problems requires the numerical solution of the elasticity problem on a large 3D domain. A sufficiently fine computational mesh is required to obtain the elastic deformation solution to the necessary accuracy, and hence a sufficiently accurate EHL point contact solution. This paper discusses the accuracy of an EHL point contact solution over different finite element meshes. We present a family of efficient 3D meshes which can be used to calculate accurate EHL point contact solutions at a minimal computational cost. This paper also illustrates the fact that the unstructured hierarchical meshes can lead to a poor quality EHL solution unless an appropriate post-processing, smoothing, technique is applied.

KEYWORDS: elastohydrodynamic lubrication; finite element method; linear elasticity; fully coupled approach; efficient meshes, hierarchical meshes

1 INTRODUCTION

Elastohydrodynamic lubrication (EHL) deals with the behaviour of lubricant film between the moving components of mechanical systems. The shape of lubricant film is determined by the

^{*}Correspondence to: Sarfraz Ahmed, School of Computing, University of Leeds, Leeds, LS2 9JT, UK. Email: scsa@leeds.ac.uk

geometry of contacting elements as well as the lubricant properties. If the pressure generated inside the lubricant film is sufficient then the contacting elements will deform elastically and hence define a new shape of lubricant film. This class of problem is known as elastohydrodynamic lubrication.

Since the shape of an elastohydrodynamic lubrication film depends only upon the elastic deformation of contact surfaces, if we are only interested in the film thickness, and the associated pressure profile through the contact, then we need only compute the elastic deformation of the surfaces themselves. Most traditional approaches e.g. [1–5] exploit this by computing the elastic deformation of the contact surfaces using a half-space approach, which is based upon an analytical solution of the elasticity equations on a semi-infinite domain. A number of efficient numerical techniques have been developed, such as the multigrid technique [1] which provided a faster convergence rate and hence reduced the computational cost. Further computation time reductions were achieved by Brandt and Lubrecht [2] introducing the Multilevel Multi-Integration (MLMI) technique, in which computation of the elastic deformation integral was accelerated. This was further developed by Venner [3, 6], Nurgat [4] and Goodyer [5]. These methods limit the discretization process to regular structured rectangular meshes using low order (usually finite difference) approximations. Furthermore, these methods are also based on a loose coupling between the governing equations (the Reynolds equation, the film thickness equation and a load balance equation), which can lead to a relatively slow convergence rate due to loss of information during the iterative link between the pressure and film thickness solutions. Nevertheless, an efficient multigrid and MLMI combination still represents one of the most effective numerical procedures for computing the pressure and film thickness to date.

An alternative to the loose coupling is the full-system approach, which consists in solving the discretized governing EHL equations simultaneously. A Newton-Raphson full system approach was first used by Oh and Rhode [7]. This method ensures the convergence of solution in few outer iterations, still based on the half-space approach for the elastic deflection. The drawback of this approach however is that use of the half-space solution requires information from all points in the domain to calculate the deflection at each point, which makes the Jacobian matrix dense. Finally, for heavy loads, the Jacobian matrix becomes almost singular, which can make it very hard to reach the solution. From 2000, a “Differential deflection method”, also based on the half-

space approach, was introduced by Evans, Hughes and co-workers [8–11]. Here, derivatives are taken of the deflection to represent it as a second order differential system. The advantage of this method is that it requires information from comparatively fewer points in the domain to calculate the elastic deflection at each point. This leads to a less dense matrix. Recently, Habchi [12–14] extended this full-system approach further by discarding the half-space approximation and solving a classical linear elasticity equation on a finite domain to calculate the elastic deflection. This equation only uses the information at the neighbouring points to calculate the elastic deflection at a point in the domain, so the resultant matrix is highly sparse and it is possible to reach the solution (even up to moderately high loads) without any special treatment for convergence.

It is important to note that this full-system approach is significantly more expensive than the classical MLMI/Multigrid approach due to the additional dimension of the linear elasticity model. However, the numerical solution of the classical linear elasticity system provides considerably more information about the solution than is available from the half-space approximation. In particular, the elastic deformation is computed throughout the contacting elements: it can therefore be used to provide engineers with further information such as stresses, which are not available using the traditional half-space approach. The reason for the increased computational cost is that the linear elasticity equation needs to be solved in a 2D domain for line contact problems, and a 3D domain for point contact problems. In a finite element solution of the linear elasticity equations, the greater the number of mesh points, the more precise the solution will be. This however leads to a significant increase in the size of the discrete algebraic system to be solved. It should also be noted that a fine mesh is required in the regions where the solution requires the greatest resolution. Therefore special attention is required to choose different mesh sizes in different parts of the domain, especially in point contact problems in order to get a precise solution with minimal computational cost. In the work of Habchi [14] this issue is addressed by dividing the elasticity domain into three distinct regions.

In this paper we seek to address the issue of the high computational cost of the point contact EHL case using the elasticity approach with an optimal preconditioning strategy [15]. In particular, we investigate the use of different mesh sizes in different parts of the 3D domain to get a sufficiently accurate elastic deformation with as few degrees of freedom as possible. This investigation is empirical and is based upon the comparison of numerical solutions computed on

different meshes. In conclusion, we present a family of efficient meshes which provide a sufficiently accurate elastic deformation at a minimal cost. The efficiency of these meshes are further justified by comparing the EHL solution with previously published results [3]. Finally, this paper also addresses a number of important issues that arise regarding the quality of unstructured hierarchical meshes.

2 MATHEMATICAL MODEL AND DISCRETIZATION TECHNIQUES

In this section we present the mathematical model of EHL point contact problems. Following the work of Habchi [12–14], the linear elasticity equation is used to compute the elastic deformation of the contacting elements. These equations are presented in the non-dimensional form. A finite element (FE) discretization of the Reynolds equation, the linear elasticity equation and the load balance equation is discussed separately.

2.1 Mathematical model

In this subsection we present an EHL model in non-dimensional form e.g see [6]. Moreover, an equivalent geometry of an EHL model is considered in this work. The equivalent geometry models the contact between two surfaces by an elastic surface and a plane where the elastic surface contains the total elastic properties of both contacting elements, and hence the solution will provide total elastic deformation of both contacting surfaces.

Our isothermal EHL model consist of three equations: the Reynolds equation, the film thickness equation and the load balance equation.

The Reynolds equation, which governs the pressure distribution through the contact reads:

$$\frac{\partial}{\partial X} \left(\epsilon \frac{\partial P}{\partial X} \right) + \frac{\partial}{\partial Y} \left(\epsilon \frac{\partial P}{\partial Y} \right) - \frac{\partial}{\partial X} (\bar{\rho} H) = 0, \quad (1)$$

where $\epsilon = \frac{\bar{\rho} H^3}{\bar{\eta} \bar{\lambda}}$, P and H are the dimensionless, unknown, pressure and film thickness respectively. Also $\bar{\rho}$ and $\bar{\eta}$ are the dimensionless density and viscosity of the lubricant and $\bar{\lambda}$ is a dimensionless speed parameter. In this work the Roelands [16] viscosity model and the Dowson

and Higginson [17] density model are used, however there is nothing that limits our approach to these models. In this work, Moes parameters L and M are used to describe an EHL case. A detailed descriptions of these parameters can be found, for example, in [6].

Generally, it is assumed that, at the boundary of the contact region Ω_c , the pressure inside the lubricant is equal to the ambient pressure. Pressure lower than the vapour pressure is physically unacceptable, thus the fluid will evaporate and the pressure will remain equal to the vapour pressure. This process is called cavitation [3, 18, 19], and since both the vapour pressure and the atmospheric pressure are very small compared to the pressure generated inside an EHL contact, they can be treated as zero, hence the pressure is limited from below by zero. Thus the Reynolds boundary conditions reads:

$$P \geq 0 \text{ on } \Omega_c \quad \text{and} \quad \nabla P \cdot \vec{n} = 0 \quad \text{at the cavitation boundary,}$$

where \vec{n} is the outward normal vector to the cavitation boundary. Since the exact location of this boundary is unknown prior to computing the pressure this is known as free boundary problem. A specific treatment is required to handle the free boundary problem and is discussed in the next section. See also [18–23], for example, for a more comprehensive discussion of treatments of cavitation at the boundary and within the Reynolds' domain.

The film thickness equation determines the shape of the lubricant film in the contact, for a circular point contact it reads:

$$H = H_0 + \frac{X^2 + Y^2}{2} + D(X, Y), \quad (2)$$

where D is the elastic deformation and H_0 is a central offset film thickness, while the middle term on the right-hand side defines the shape of undeformed surface.

Finally, the load balance equation is a conservation law, which ensures that the total pressure generated balances the applied load and is given by

$$\int \int_{\Omega_c} P(X, Y) d\Omega_c = \frac{2\pi}{3}. \quad (3)$$

2.2 Linear elasticity equation:

In the film thickness equation, the elastic deformation D of the contacting bodies can be modelled by solving the classical linear elasticity equation on a three dimensional domain Ω (for point contact), see Figure 1, with appropriate boundary conditions:

$$\frac{\partial}{\partial X_j} \left(C_{ijkl} \frac{\partial U_k}{\partial X_l} \right) = 0, \quad (4)$$

where repeated suffices imply summation (over the three space dimensions),

$$C_{ijkl} = \lambda \delta_{ij} \delta_{kl} + \mu (\delta_{ik} \delta_{jl} + \delta_{il} \delta_{jk})$$

and λ and μ are material properties given by

$$\lambda = \frac{\nu E}{(1 + \nu)(1 - 2\nu)}, \quad \mu = \frac{E}{2(1 + \nu)}.$$

Here δ_{ij} is the kronecker delta, whilst E is the reduced Young's modulus and ν is the reduced Poisson ratio of the material used. A detailed description is provided, for example, in [12–14]. Note that the equation (4) is solved subject to the boundary conditions:

$$\begin{cases} U = 0 & \text{at the bottom boundary } \Omega_D; \\ \sigma_n = n_j C_{ijkl} \frac{\partial U_k}{\partial X_l} = -\delta_{i3} P & \text{at the contact boundary } \Omega_C; \\ \sigma_n = 0 & \text{elsewhere.} \end{cases} \quad (5)$$

2.3 Discretization

As stated earlier, the linear elasticity equation needs to be solve on a 3D domain Ω for the point contact problems. In this work we follow Habchi [12] and select a cubic domain for the reduced geometry. In [12] it is demonstrated that a geometry of size $60 \times 60 \times 60$ is sufficiently large to provide accurate solutions, so this is adopted throughout this paper. Let $\partial\Omega$ be boundary of the domain Ω and Ω_c is part of $\partial\Omega$ that corresponds to the contact region. In this work, a standard Galerkin discretization of the Reynolds equation (in Ω_c) and the linear elasticity equation (in Ω) is considered. It should be noted that a penalty method [20] is used to handle the cavitation

boundary, thus the Reynolds equation takes the following form:

$$\nabla \cdot (\epsilon \nabla P) - \frac{\partial}{\partial X} (\bar{\rho} H) - \xi P^- = 0, \quad \text{throughout } \Omega_c, \quad (6)$$

where we impose $P = 0$ on $\partial\Omega_c$, ξ is a suitably large positive number and $P^- = \min(P, 0)$. Note that this term has no effect where $P \geq 0$, however it dominates only in the regions where $P < 0$. This term has an effect of forcing the negative pressure towards zero provided that ξ is sufficiently large. In this work ξ is chosen to be $10^6 \times h_e^2$ as suggested in [13], where h_e is the characteristic length of an element. An increase in this factor will lead to an increase in the computational work for minimal change in the solution. Moreover, while updating the density and viscosity the very small negative pressures in the cavitation regions are treated as zero.

For a weighting function W_p , the weak form of the Reynolds equation is:

$$\int_{\Omega_c} \epsilon \nabla P \cdot \nabla W_p d\Omega_c - \int_{\Omega_c} \bar{\rho} H \frac{\partial W_p}{\partial X} d\Omega_c + \xi \int_{\Omega_c} P^- W_p d\Omega_c = 0. \quad (7)$$

Similarly, for a weighting function W_u , the weak form of the linear elasticity equation is:

$$\int_{\Omega} C_{ijkl} \frac{\partial U_k}{\partial X_l} \frac{\partial W_u}{\partial X_j} d\Omega = \int_{\Gamma_t} n_j C_{ijkl} \frac{\partial U_k}{\partial X_l} W_u d\Gamma_t, \quad (8)$$

where Γ_t is part of $\partial\Omega$ corresponds to traction boundary. As shown in (5) $n_j C_{ijkl} \frac{\partial U_k}{\partial X_l}$ represents the normal traction and is given as

$$\begin{cases} n_j C_{ijkl} \frac{\partial U_k}{\partial X_l} = 0 & \text{when } \Gamma_t = \partial\Omega - \Omega_c \\ n_j C_{ijkl} \frac{\partial U_k}{\partial X_l} = -\delta_{i3} P & \text{when } \Gamma_t = \Omega_c \end{cases}$$

Equation (8) can therefore be written as:

$$\int_{\Omega} C_{ijkl} \frac{\partial U_k}{\partial X_l} \frac{\partial W_u}{\partial X_j} d\Omega + \int_{\Omega_c} \delta_{i3} P W_u d\Omega_c = 0. \quad (9)$$

Consider a partition of Ω into N_u tetrahedral elements, $\{\Omega_e\}$, such that N_p of these elements have triangular faces on Ω_c (and these triangular faces form a partition of Ω_c). Let $\{\Omega_{ce}\}$ be the set of these N_p triangles and define \mathcal{P}_u^h and \mathcal{P}_p^h to be piecewise linear finite element spaces over

$\{\Omega_e\}$ and $\{\Omega_{ce}\}$ respectively.

Equations (7) and (9) can be written as a sum over these elements:

$$\sum_{\Omega_{ce}=1}^{N_p} \left(\int_{\Omega_{ce}} \epsilon \nabla P \cdot \nabla W_p d\Omega_{ce} - \int_{\Omega_{ce}} \bar{\rho} H \frac{dW_p}{dX} d\Omega_{ce} + \xi \int_{\Omega_{ce}} P^- W_p d\Omega_{ce} \right) = 0, \quad (10)$$

$$\sum_{\Omega_e=1}^{N_u} \int_{\Omega_e} C_{ijkl} \frac{\partial U_k}{\partial X_l} \frac{\partial W_u}{\partial X_j} d\Omega_e + \sum_{\Omega_{ce}=1}^{N_p} \int_{\Omega_{ce}} \delta_{i3} P W_u d\Omega_{ce} = 0. \quad (11)$$

In each element Ω_{ce} , P in equation (10) is approximated by:

$$P \approx P^e = \sum_{j=1}^3 N_j^e P_j^e \quad (12)$$

where N_j^e are local linear basis functions and P_j^e are nodal values of P within the element. So replacing P in equation (10) with the approximation given in equation (12) and W_p with N_i^e for $i = 1, \dots, 3$, followed by the usual finite element assembly process, leads to a discrete system of n_p nonlinear equations, where n_p is total number of nodes in Ω_{ce} , excluding boundary nodes.

Similarly, in each element Ω_e , U in equation (11) is approximated by:

$$U^e = \sum_{q=1}^4 W_q^e U_q^e \quad (13)$$

where W_q^e are local linear basis functions and U_q^e are nodal values of the displacement U within the element. So replacing U in equation (11) with the approximation given in equation (13), P with the approximation given in equation (12) and W_u with $(W_q^e, 0, 0)^T$, $(0, W_q^e, 0)^T$ and then $(0, 0, W_q^e)^T$ for $q = 1, \dots, 4$, leads to a discrete system of $3 \times n_u$ linear equations, where n_u is total number of nodes in Ω excluding Dirichlet boundary nodes.

Finally, the discrete form of the load balance equation is obtained by using the finite element assembly of the approximation given in (12):

$$\sum_{\Omega_{ce}=1}^{N_p} \int_{\Omega_{ce}} \sum_{j=1}^3 N_j^e P_j^e d\Omega_{ce} - \frac{2\pi}{3} = 0. \quad (14)$$

2.4 Solution procedure

In this work, a fully coupled solution approach is considered. This involves the direct coupling of all of the discrete systems arising from the finite element discretization of the EHL equations to form a nonlinear system of equations for all unknowns. This is solved in one pass. Thus, no under-relaxation is required and no extra treatment is required to achieve convergence for heavily loaded cases (provided a sufficiently good initial guess is used). The discretized systems discussed in the previous subsection can be written in the following matrix form:

$$\begin{cases} \mathbf{R}_P(\mathbf{P}, \mathbf{U}, H_0) & = 0 \\ \mathbf{R}_U(\mathbf{P}, \mathbf{U}) & = 0 \\ R_{H_0}(\mathbf{P}) & = 0 \end{cases} \quad (15)$$

where \mathbf{R}_P represents the system of n_p nonlinear equations arising from the discretization of Reynolds equation, \mathbf{R}_U is the linear system of $3 \times n_u$ equations arising from discretization of the linear elasticity equation and R_{H_0} is the scalar residual of the discretized load balance equation (14). Similarly, \mathbf{P} is a vector of the n_p unknown pressure coefficients, \mathbf{U} is a vector of the $3 \times n_u$ unknown displacement components and H_0 is the unknown central offset. In this work, a Newton-Raphson procedure is applied to system (15) to yield the following linear system at each outer iteration:

$$\begin{bmatrix} \frac{\partial \mathbf{R}_P}{\partial \mathbf{P}} & \frac{\partial \mathbf{R}_P}{\partial \mathbf{U}} & \frac{\partial \mathbf{R}_P}{\partial H_0} \\ \frac{\partial \mathbf{R}_U}{\partial \mathbf{P}} & \frac{\partial \mathbf{R}_U}{\partial \mathbf{U}} & \mathbf{0} \\ \frac{\partial R_{H_0}}{\partial \mathbf{P}} & \mathbf{0}^T & 0 \end{bmatrix} \begin{bmatrix} \delta \mathbf{P} \\ \delta \mathbf{U} \\ \delta H_0 \end{bmatrix} = \begin{bmatrix} -\mathbf{R}_P \\ -\mathbf{R}_U \\ -R_{H_0} \end{bmatrix}. \quad (16)$$

Starting with an initial estimate for the solution, the Newton procedure consists of solving the linearized system (16) at each Newton iteration and this update is added to the solution obtained at the previous iteration, to provide an improved solution. This process is repeated until convergence is achieved. If the initial guess is not sufficiently accurate then some under-relaxation may be required to achieve the convergence. In this work, we only used a Hertzian pressure profile as an initial guess for pressure and no under-relaxation was required to reach the converged solution

for the loads reported here.

Since the Reynolds equation exhibits an oscillatory behaviour in the pressure solution for heavily loaded cases (see [1, 6] for example), in order to get a stabilized solution a Streamline Upwind Petrov Galerkin (SUPG) method [24] has been used. To explain the implementation, let us rewrite equation (1) in the classical convection-diffusion form as follow:

$$-\nabla \cdot (\epsilon \nabla P) + H \frac{\partial \bar{\rho}}{\partial P} \frac{\partial P}{\partial X} + \bar{\rho} \frac{\partial H}{\partial X} = 0,$$

which may be expressed as

$$-\nabla \cdot (\epsilon \nabla P) + V \cdot \nabla P + Q = 0, \quad (17)$$

where $V = (V_1, V_2) = (H \frac{\partial \bar{\rho}}{\partial P}, 0)$ and $Q = \bar{\rho} \frac{\partial H}{\partial X}$. The terms in equation (17) are known as the diffusion, convection and source terms respectively. The SUPG method applied to this kind of problem consists of choosing the weighting function W_p in equation (10) (excluding penalty term) of the form:

$$W_p = N_p + \alpha_s \frac{h_e}{2|V|} V \cdot \nabla N_p$$

with

$$\alpha_s = \coth(Pe) - \frac{1}{Pe}, \quad Pe = \frac{|V|h_e}{2\epsilon},$$

where h_e is the characteristic length of an element and Pe is the local Peclet number of the element e . In the Galerkin procedure, oscillations will occur whenever $|Pe| > 1$ however these are damped by the SUPG approach. For more details, see for example [13, 24, 25]. Note that the extra terms (introduced by SUPG approach) have no effect on the accuracy of a converged solution in the limit as the mesh size goes to zero.

Note that the solution of the coupled linear system (16) is the most expensive part of the solution procedure. In [14] a sparse direct method is used. Whilst very efficient for line contact problems this does require significant memory and CPU resource for point contact problems. Furthermore, since the solution of (16) is only required as part of an outer iteration it is not generally necessary to solve it exactly, i.e. it is only necessary to solve the linear system (16) to a

sufficient precision in order to determine a good Newton update to achieve convergence of the nonlinear system (15). In this work therefore we have made use of a preconditioned GMRES method [26] to solve (16) at each Newton iteration. The key feature that makes this approach computationally competitive is the choice of preconditioner and in [15] we describe a preconditioner which allows both very fast convergence and a very rapid application at each inner iteration. This is based upon approximating the $\frac{\partial \mathbf{R}_U}{\partial \mathbf{U}}$ block in (16) by a single algebraic or geometric multigrid V-cycle [27–29] and using a fast sparse direct solver [30] for the $\frac{\partial \mathbf{R}_P}{\partial \mathbf{P}}$ block of the preconditioner. Results presented in [15] show that this approach substantially out-performs the application of a sparse direct solver to the whole of (16), both in terms of memory and of CPU requirements.

3 EHL RESULTS

For the point contact problems considered here, the Reynolds equation needs to be solved on a 2D domain and the elasticity equation on a 3D domain. As previously mentioned, following Habchi [12], we let Ω represent a 3D domain $-30 \leq X \leq 30$; $-30 \leq Y \leq 30$; $-60 \leq Z \leq 0$. In [12] experiments were undertaken on different dimensions leading to the said dimension being adopted in their work. In this section, we first discuss the accuracy of the elastic deformation solution by defining suitable meshes and give a comparison against solutions obtained by using very fine meshes. These tests have been carried out first using a Hertzian pressure profile and then assuming a typical EHL pressure profile, though the results presented here are only for the EHL pressure profile. The test cases considered in this work are described in the Table 1. These test cases are taken from [3] in order to establish a comparison of the current model with a finite difference based model so as to validate the calculated point contact results.

It should be noted that the fine mesh cases used for comparison of solutions lead to very large computational problems and it has only been practical to solve these large problems by developing an efficient preconditioned GMRES solver [15]. This solver uses a block-wise preconditioning strategy. The preconditioning of the elasticity block is done using AMG preconditioning which is designed to be of order $O(n)$ and the preconditioning of the Reynolds block is done

using an efficient sparse direct solver. We discuss full details of the performance of this solver in [15].

Ω_c is the part of the boundary of the 3D domain which corresponds to the contact region and is chosen to be of dimension $-4.5 \leq X \leq 1.5; -3 \leq Y \leq 3$. Note that three resolution cases, named Resolution 1, 2 and 3, are used in this work, corresponding to regular grids of 64×64 , 128×128 and 256×256 points in Ω_c respectively.

Throughout this section meshes have been generated using the open source software NET-GEN [31]. This allows meshes of a given local spacing to be defined, as well as permitting hierarchical mesh refinement to take place. Moreover, it allows one to perform mesh optimization over the meshes resulting from hierarchical mesh refinement.

3.1 Accuracy of the elastic deformation

The pressure generated inside the lubricant film is high enough in the contact region to lead to a significant elastic deformation while, on the other hand, the pressure outside the contact region is relatively low. Moreover, the precision of the computed elastic deformation is most important in the contact region, since this is where it has most effect on the Reynolds equation. Hence, we propose that a fine 3D mesh is required in the contact region up to a certain depth, but not in the whole elasticity domain. Nevertheless, a suitable mesh size needs to be defined outside the contact region in order to get a sufficiently accurate solution throughout the whole domain.

Here, we present selected meshes which give a sufficiently accurate elastic deformation solution at as low a cost as possible. In order to show the effectiveness of these meshes, the elastic deformation solution is compared against the solution obtained on very fine meshes. In the case of fine meshes, we split the 3D domain into two regions. The first region is of dimension $-4.5 \leq X \leq 4.5; -3 \leq Y \leq 3; -3 \leq Z \leq 0$ and the second region is the remainder of the domain. A mesh size corresponding to different resolution cases is adopted everywhere in the first region and a mesh size of 0.5 is used in the remaining region. A view (XY plane, where $Z = 0$) of the top of the domain is shown in figure 2. For the sake of simplicity, the notations $R1$ and $R2$ are used to represent these two different regions in the domain, $R1$ representing the whole domain, and $R2$ representing the central region of dimension

$-4.5 \leq X \leq 4.5; -3 \leq Y \leq 3; -3 \leq Z \leq 0$. It should be noted that the length of $R2$ is chosen $-4.5 \leq X \leq 4.5$ instead of $-4.5 \leq X \leq 1.5$ (see definition of Ω_c above) in order to get a sufficiently accurate elastic deformation solution. We carried out different experiments to ensure that any increase in the depth of $R2$ and any further decrease in the mesh size adopted in the remaining region does not lead to any significant improvement in the accuracy of the elastic deformation solution. Note that this two-region strategy for defining fine meshes for the three resolution cases considered leads to 3505403, 4950405 and 15802299 nodes in the mesh respectively.

Having established meshes to act as a benchmark for each of the three resolutions to be considered, we now seek to define meshes with fewer degrees of freedom that are able to yield results of similar accuracy. To do this we split the 3D domain into four regions. The first two regions are hemispherical regions with radii ‘1.5’ and ‘15’ respectively. The third region is a cube of dimensions $-20 \leq X \leq 20; -20 \leq Y \leq 20; -40 \leq Z \leq 0$ while the fourth region is the remaining region of the domain. The choice of first region is based on the fact that this includes the region where the pressure values are most significant (especially in the inlet region). The choices of regions 2 and 3 are based upon a large number of different computational experiments that are not repeated here. A selected resolution (Mesh size 1) is specified for all points inside the region 1 and a suitable mesh size (Mesh size 2) is defined for points on the curved boundary of region 2. For all other interior points of region 2, linear interpolation is used to define a mesh size for each point. It should be noted that in the remaining regions of the domain (outside of region 2), different large mesh sizes (Mesh size 3 in region 3 and Mesh size 4 in region 4) are used depending upon the resolution used in the most central region. The mesh sizes 1 to 4 (for the four regions respectively) for each resolution case are given in the Table 2, defining the proposed meshes. Note that the purpose of defining region 3 (particularly for resolution-3) is to control the huge increase in number of nodes in the mesh without significantly affecting the overall accuracy of solution.

The root mean square error (RMSE) for the displacement in all three selected resolution cases, along with their fine (benchmark) cases, are calculated with respect to the fine case of resolution 3 and are given in the Table 3. These figures are obtained by comparing the computed solution on the given mesh against the best available solution, on the finest available mesh. One can see

that the selected cases lead to a small fraction of the nodes compared to their corresponding fine cases (with the same resolution in the contact region) without significantly affecting the accuracy of the solution. In particular, for Resolution 1 and Resolution 2 the errors in the selected cases are of the same order of magnitude (less than a factor of 2 difference) as those based on the benchmark meshes of the same resolution. Moreover, a view of the elastic deformation solution using the fine and selected cases at resolution-1 along the central line in Ω_c (where $Y = 0$) is given in Figure 3, which also shows that both results are extremely close to each other.

3.2 Point contact results

In this subsection, a comparison of the fully-coupled finite element solver is made with published results using the integral approach in a finite difference based model. This will enable us to validate the calculated point contact results. We have split this comparison into two phases, one using the very fine meshes and the other using the more efficient meshes described above.

In the first part, our benchmark meshes lead to the same mesh size (corresponding to three different resolutions) everywhere in the contact region (Ω_c), which therefore provides a fair comparison with the finite difference based model [3]. A comparison of these results obtained for the Test Case 1 with the finite difference based model is given in Table 4 in terms of central and minimum film thicknesses (this is the data provided in [3]). It should be noted that the number marked ‘ n_p ’ represents the number of pressure unknowns in the contact region and ‘Total dof’ represents total unknowns of the fully coupled system. It can be seen that the calculated results are very close to that of the finite difference based model. The difference in the two solutions get smaller and smaller as we switch to higher resolutions. Moreover, it should be noted that both models use totally different approaches, therefore a small difference in the solutions is expected even though they appear to converge to the same result. The main drawback of these results is the use of very fine meshes, leading to very large discrete problems, which are very expensive from a computational point of view.

In the second part, we are comparing the previous computed results with those computed over the selected meshes which were determined, as described in the previous subsection, based upon numerical experiments to ensure a sufficiently accurate elastic deformation solution with

a significantly reduced computational cost. This comparison is given in Table 5. One can see that the accuracy of the solution is not significantly affected (relative to the overall discretization error) while keeping in mind the total decrease in the size of problem. For example in case 3 of Table 5, a reduction of 45M degrees of freedom (dof) leads to a very small drop in the accuracy of solution. In particular, in the selected cases, the same order of magnitude in error is observed as with the fine cases.

A similar trend in the solutions is observed for Test Case 2 which is a comparatively more heavily loaded case. Table 6 provides a comparison of results obtained on fine meshes against the finite difference based results [3]. It is evident that the calculated values are again close to those of finite difference based model and that they again appear to converge to the same result. Similarly, Table 7 provides a comparison of fine case results with those computed over the selected meshes. Again it can be seen that the accuracy of the solution is not significantly affected for this loaded case (Test Case 2) while computing the solution over the selected meshes. This experiment (and further experiments undertaken but not repeated here) provides further evidence that the mesh selection approach proposed in this work may be applied across a range of EHL cases.

3.3 Hierarchical Meshes

In addition to the local mesh resolution, another important factor which affects the accuracy of a solution of a problem is the quality of mesh used [32, 33]. In other words, optimizing the quality of a mesh prior to computing the solution of a problem can improve the accuracy of the solution. In this subsection, this aspect of the solution process is considered by computing the EHL solution over different meshes of resolution 2. In mesh optimization, some measure of the quality of the mesh is improved by modifying the mesh in different ways. The mesh optimization in NETGEN [31] includes local reconnection via edge and face swaps, local node movement, and some collapsing of elements. The metric used is based upon minimizing an error functional which quantify the quality of the mesh.

For this paper an experiment is carried out for the Test Case 1 in which an optimized coarse mesh is chosen as an initial mesh. Three cases are then considered. In the first case (Case 1), two levels of uniform refinement is applied to the initial mesh. Each refinement involves the

division of each tetrahedral element into 8 child tetrahedra, growing the number of elements eight times at each refinement level. The division of each tetrahedron is done in two phases, the first leading to the removal of four corners, leaving an octahedron behind. This octahedron is further divided to produce four new tetrahedra. There are three choices of diagonals which can be used to divide this octahedron. In this case, we have used the longest diagonal [34], however other choices [35] are possible. In the second case (Case 2), the two levels of refinement are carried out using NETGEN [31]. Finally, an optimization is performed (within NETGEN [31]) over the mesh obtained in Case 2 leading to Case 3.

It may be observed that Case 1 leads to a poor quality solution since unphysical oscillations are clearly visible in the pressure solution, see Figure 4. On the other hand, Case 2 yields a slightly better solution (with fewer oscillations) than that of Case 1, while Case 3 leads to a smooth pressure profile. It should be noted that the number of degrees of freedom for the first two cases are the same (710906) as a result of the uniform refinement procedures, while in Case 3 this number is 670577. This slight reduction is due to the collapsing of nodes, edges, faces and elements that takes place during the mesh optimization process. The key observation however is that the smoother, optimized, mesh can yield a better accuracy in the solution than that of a non-optimized mesh with more nodes. Moreover, in this example we have selected the initial mesh such that two levels of refinement produce an equivalent mesh to the selected case of resolution 2 (see previous subsection). The RMSE of the pressure and film thickness solutions for these different resolution 2 cases are calculated with respect to the fine case of resolution 3 and are given in Table 8. It can be seen that the RMSE of each of the film thickness solutions are smaller and comparatively more closer to each other than the pressure RMSEs. The accuracy of the pressure profile increases while switching from Case 1 to Case 3 and in Case 3 it is even slightly improved than that of the selected case. Moreover, it is apparent that the accuracy of the pressure and film thicknesses solutions is not significantly affected as compared to the solutions computed on the very fine reference mesh with a huge number of degrees of freedom (14834838).

4 CONCLUSION

In this paper, we used a fully coupled approach to the solution of EHL point contact problems with a finite element approximation to the linear elasticity problem as an alternate to the analytic half-space method. This approach was first used by Habchi et al. [12–14] though they used a direct solver for the linearized system (16) at each Newton step. They also used higher order elements in order to get a reduced system with a desired accuracy. In order to overcome the memory and CPU restrictions for the larger 3D problems, we have developed a preconditioned iterative fully coupled solver [15] and applied it in this work, with low order finite elements.

The contribution of this paper is to investigate the accuracy of the elastic deformation solution, as well as the complete point contact EHL results, over a number of different finite element meshes for the linear elasticity problem. It has been possible to show that a judicious choice of these finite element meshes can allow a substantial reduction in the total number of degrees of freedom without reducing the overall accuracy relative to the discretization error in the Reynolds equation solution. In the specific example included here this results in a reduction in CPU of about 96% (from 31681s to 1242s) and a reduction in memory of about 96% (from 34Gb to 1.5Gb). The results presented in this paper have been found to be accurate over a relatively small range of EHL problems, however, it requires a systematic study over a wider range of cases to demonstrate, as we expect, its applicability in full. Moreover, by defining four regions of the elasticity domain we have provided a general methodology for selecting a suitable elastic mesh for a range of EHL point contact problems. Note that if the surface roughness is taken into account then a finer mesh in the contact region (high pressure region) may be required and this may therefore affect the mesh sizes close to the central contact region accordingly. Nevertheless the approach used here would still be applicable.

The solution algorithm [15] used here is based upon the use of linear elements since AMG methods are well developed and much more efficient for linear elements than higher order elements. The reduced problem sizes reported here are quite promising, however a large number of elements were still required to achieve a desired accuracy. On the other hand, the use of higher order elements would be more accurate [14] and thus would allow the use of coarse elements throughout the domain to achieve the equivalent accuracy. However, the development of an ef-

efficient solution algorithm, like preconditioned GMRES presented in [15], is required in order to fully benefit from the use of higher order elements in further mesh density optimization. Nevertheless, this work should extend to higher order elements since it has been shown in a recent work [36] that the AMG approach works well for linear elasticity with higher order finite elements.

A further observation that we provide in this work is that the use of unstructured hierarchical meshes without appropriate mesh optimization can lead to poor quality EHL results. This is likely to be an important observation in future work when we will seek to make use of local error estimation to control the mesh refinement locally in order to automate the generation of the linear elasticity finite element meshes.

ACKNOWLEDGEMENTS

The first author thanks to Higher Education Commission (HEC), Pakistan for their financial support that has allowed this research to be undertaken at the University of Leeds.

References

- [1] Lubrecht AA. Numerical solution of the EHL line and point contact problem using multigrid techniques [PhD thesis]. University of Twente. Enschede, The Netherlands; 1987.
- [2] Brandt A, Lubrecht AA. Multilevel Matrix Multiplication and Fast Solution of Integral Equations. *J Comput Phys.* 1990;Vol 90 (2):pp. 348–370.
- [3] Venner CH, Lubrecht AA. *Multilevel Methods in Lubrication.* Elsevier, Netherlands; 2000.
- [4] Nurgat E. Numerical Methods in Lubrication Modelling [PhD thesis]. University of Leeds. Leeds, UK; 1997.
- [5] Goodyer CE. Adaptive Numerical Methods for Elastohydrodynamic Lubrication [PhD thesis]. University of Leeds. Leeds, UK; 2001.
- [6] Venner CH. Multilevel Solution of the EHL Line and Point Contact Problems [PhD thesis]. University of Twente. Enschede, The Netherlands; 1991.

- [7] Oh KP, Rohde SM. Numerical solution of the point contact problem using the finite element method. *International Journal for Numerical Methods in Engineering*. 1977;Vol 11:pp. 1507–1518.
- [8] Evans HP, Hughes TG. Evaluation of Deflection in Semi-Infinite Bodies by a Differential Method. *Proc IMechE J Mech Engrng Sc*. 2000;Part C, Vol 214:pp. 563–584.
- [9] Hughes TG, Elcoate CD, Evans HP. Coupled Solution of the Elastohydrodynamic Line Contact Problem Using a Differential Deflection Method. *Proc IMechE J Mech Engrng Sc*. 2000;Part C, Vol 214:pp. 585–598.
- [10] Holmes MJA, Evans HP, Hughes TG, Snidle RW. Transient Elastohydrodynamic Point Contact Analysis Using a New Coupled Differential Deflection Method. Part I: Theory and Validation. *Proc IMechE J Mech Engrng Sc*. 2003;Part J, Vol 217:pp. 289–303.
- [11] Holmes MJA, Evans HP, Hughes TG, Snidle RW. Transient Elastohydrodynamic Point Contact Analysis Using a New Coupled Differential Deflection Method. Part II: Results. *Proc IMechE J Mech Engrng Sc*. 2003;Part J, Vol 217:pp. 305–321.
- [12] Habchi W, Eyheramendy D, Vergne P, Morales-Espejel G. A Full-System Approach of the Elastohydrodynamic Line/Point Contact Problem. *ASME J Tribol*. 2008;130, 021501.
- [13] Habchi W, Eyheramendy D, Vergne P, Morales-Espejel G. Stabilized Fully-Coupled Finite Elements for elastohydrodynamic Lubrication Problems; 2010. *Adv Eng Softw*, In press(2010).
- [14] Habchi W. A Full-System Finite Element Approach to Elastohydrodynamic Lubrication Problem: Application to Ultra-Low-Viscosity Fluids [PhD thesis]. University of Lyon. France; 2008.
- [15] Ahmed S, Goodyer CE, Jimack PK. An efficient preconditioned iterative solution of fully-coupled elastohydrodynamic lubrication problems. Submitted for publication in *Applied Numerical Mathematics* (2011);.
- [16] Roelands CJA. Correlational Aspects of the Viscosity-Temperature-Pressure Relationship of Lubricating Oils [PhD thesis]. Technische Hogeschool Delft. The Netherlands; 1966.
- [17] Dowson D, Higginson GR. *Elastohydrodynamic Lubrication*. Pergamon Press, Oxford; 1977.
- [18] Floberg L. *Cavitation in Lubricating Oil Films*. Elsevier, Amsterdam; 1964.
- [19] Elrod HG. A Cavitation Algorithm. *Journal of Lubrication Technology-Transactions of the ASME*. 1981;103:350–354.
- [20] Wu SR. A penalty formulation and numerical approximation of the Reynolds-Hertz problem of elastohydrodynamic lubrication. *International Journal of Engineering Science*. 1986;Vol. 24(No.6):1001–1013.

- [21] Thatte A, Salant RF. Transient EHL Analysis of an Elastomeric Hydraulic Seal. *Tribology International*. 2009;42(10):1424–1432.
- [22] Thatte A, Salant RF. Visco-Elastohydrodynamic Model of a Hydraulic Rod Seal During Transient Operation. *Journal of Tribology*. 2010;132(4):041501–1 – 041501–13.
- [23] Payvar P, Salant RF. A Computational Method for Cavitation in a Wavy Mechanical Seal. *Journal of Tribology*. 1992;114(1):199–204.
- [24] Brooks AN, Hughes TJR. Streamline-Upwind/Petrov-Galerkin Formulations for Convective Dominated Flows with Particular Emphasis on the Incompressible Navier-Stokes Equations. *Comp Meth Appl Mech Engrng*. 1982;Vol. 32:pp.199–259.
- [25] Zienkiewicz OC, Taylor RL. *The Finite Element Method*, 5th edition, Volume 3: Fluid Dynamics. Butterworth-Heinmann, Oxford; 2000.
- [26] Saad Y, Schultz MH. GMRES: a generalized minimal residual algorithm for solving nonsymmetric linear systems. *SIAM Journal on Scientific and Statistical Computing*. 1986;7:856–869.
- [27] Boyle J, Mihajlovic M, Scott J. HSL_MI20: An efficient AMG preconditioner for finite element problems in 3D. *International Journal for Numerical Methods in Engineering*. 2010;82(1):64–98.
- [28] Briggs WL, Henson VE, McCormick SF. *A Multigrid Tutorial*. Society for Industrial and Applied Mathematics; 2000.
- [29] Trottenberg U, Oosterlee CW, Schuller A. *Multigrid*. Academic Press; 2001.
- [30] Davis TA. Algorithm 832: UMFPACK, an unsymmetric-pattern multifrontal method. *ACM Transactions on Mathematical Software*. June 2004;30(2):196–199.
- [31] Schoeberl J. Netgen, an advancing front 2d/3d-mesh generator based on abstract rules. *Comput Visual Sci*. 1997;1:41–52.
- [32] Berzins M. Solution-based mesh quality for triangular and tetrahedral meshes. In: *Proceedings of the Sixth International Meshing Roundtable*. Sandia National Laboratories; 1997. p. 427–436.
- [33] Berzins M. Mesh quality - geometry, error estimates or both? In: *Proceedings of the Seventh International Meshing Roundtable*. Sandia National Laboratories; 1998. p. 229–237.
- [34] Speares W, Berzins M. A 3d unstructured mesh adaptation algorithm for time-dependent shock-dominated problems. *International Journal for Numerical Methods in Fluids*. 1997;25(1):81–104.
- [35] Ong ME. Uniform refinement of tetrahedron. *Siam Journal of Scientific Computing*. 1994;15(5):1134–1144.

- [36] Xiao Y, Shu S, Zhao T. A geometric-based algebraic multigrid method for higher-order finite element equations in two-dimensional linear elasticity. *Numerical Linear Algebra with Applications*. 2009;16:535–559.

List of Figures

1	A view of the 3D elasticity domain Ω showing Ω_C (the contact boundary) and Ω_D (the bottom boundary)	23
2	A view of the top of the 3D domain	24
3	Elastic deformation solution along the central line in Ω_c (where $Y = 0$): Fine and Selected case of resolution-1: Test Case 1.	25
4	The shapes of pressure profile along the central line (where $Y = 0$) computed over optimized and non-optimized meshes. (a) Pressure profile: Case-1. (b) A close-up of the pressure profile: Case-1. (c) A close-up of the pressure profile: Case-2. (d) A close-up of the pressure profile: Case-3.	26

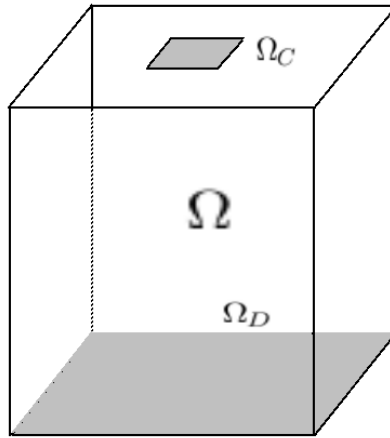


Figure 1: A view of the 3D elasticity domain Ω showing Ω_C (the contact boundary) and Ω_D (the bottom boundary)

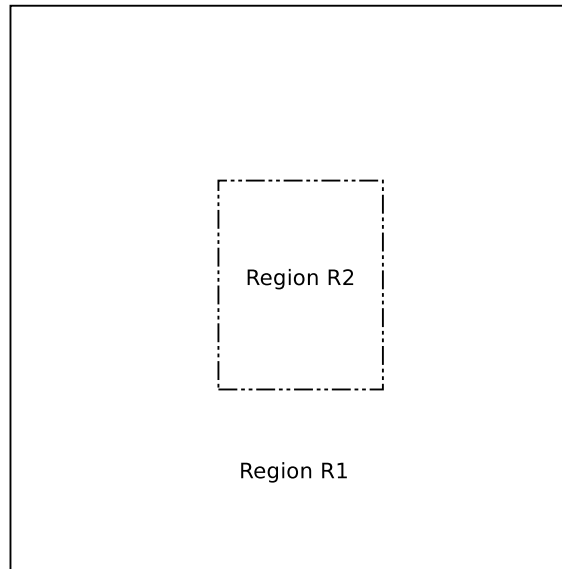
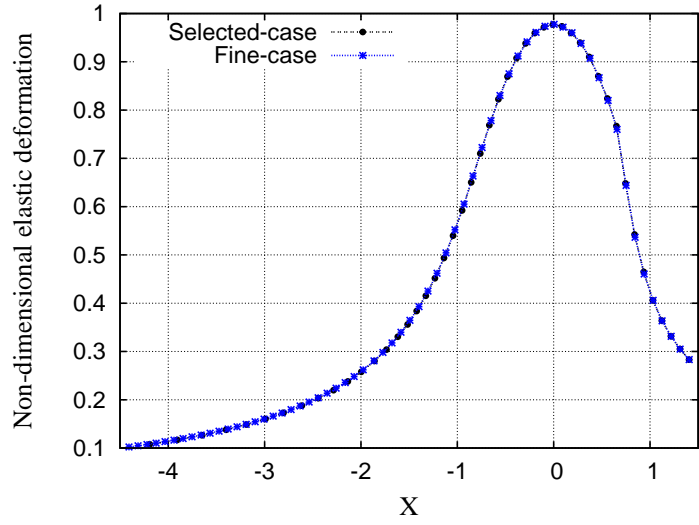
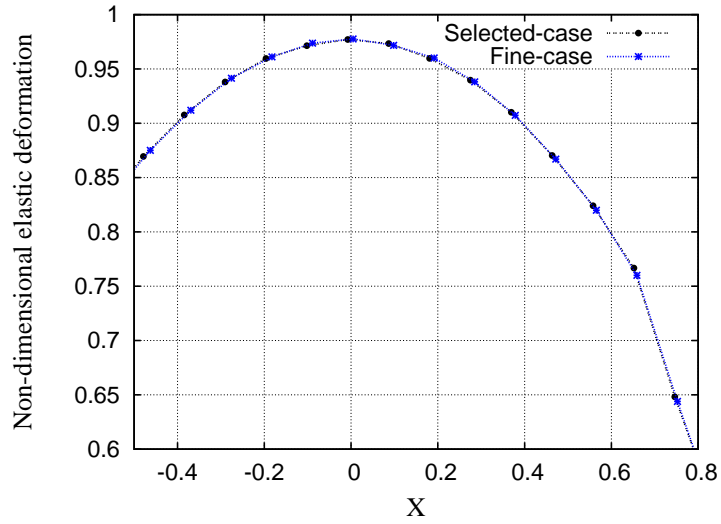


Figure 2: A view of the top of the 3D domain



(a)



(b) Zoom-in

Figure 3: Elastic deformation solution along the central line in Ω_c (where $Y = 0$): Fine and Selected case of resolution-1: Test Case 1.

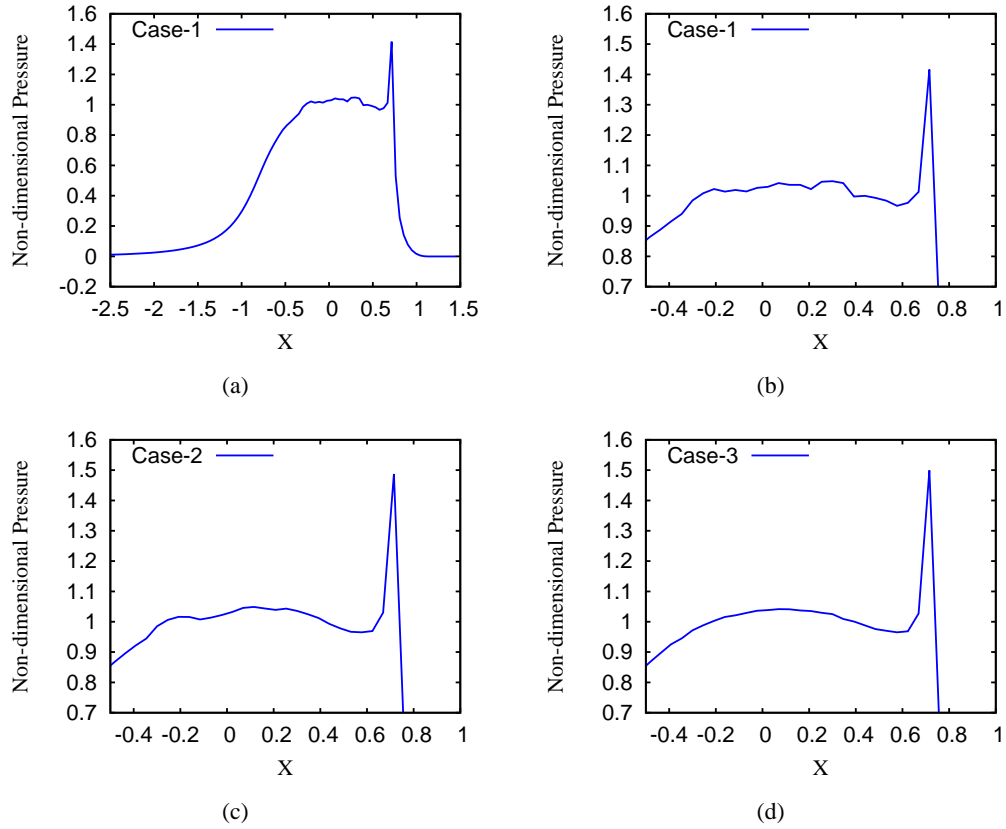


Figure 4: The shapes of pressure profile along the central line (where $Y = 0$) computed over optimized and non-optimized meshes. (a) Pressure profile: Case-1. (b) A close-up of the pressure profile: Case-1. (c) A close-up of the pressure profile: Case-2. (d) A close-up of the pressure profile: Case-3.

List of Tables

1	Non-dimensional parameters for the contact between steel surfaces [3].	28
2	A set of mesh sizes defining the selected mesh for each resolution case.	29
3	Root mean square error for the displacement in all three selected resolution cases along with their fine cases: Test Case 1.	30
4	Validation of point contact results: Test Case 1.	31
5	A comparison of point contact results over fine and selected meshes: Test Case 1.	32
6	Validation of point contact results: Test Case 2.	33
7	A comparison of point contact results over fine and selected meshes: Test Case 2.	34
8	Root mean square error of pressure and film thicknesses solutions of various resolution 2 cases with respect to the fine case of resolution 3: Test Case 1.	35

Table 1: Non-dimensional parameters for the contact between steel surfaces [3].

Parameters	Test Case 1	Test Case 2
Moes parameter, L	10	10
Moes parameter, M	20	200
Maximum Hertzian pressure, p_h	0.45GPa	0.97GPa
Viscosity index, α	$2.2 \times 10^{-8} \text{Pa}^{-1}$	$2.2 \times 10^{-8} \text{Pa}^{-1}$
Viscosity at ambient pressure, η_0	0.04 Pa s	0.04 Pa s
Total speed, u_s	1.6 m s^{-1}	1.6 m s^{-1}

Table 2: A set of mesh sizes defining the selected mesh for each resolution case.

Selected Case	Mesh size 1	Mesh size 2	Mesh size 3	Mesh size 4
Resolution-1	0.09375	1.0	4.0	4.0
Resolution-2	0.04688	1.0	2.0	2.0
Resolution-3	0.02344	0.7	1.0	2.0

Table 3: Root mean square error for the displacement in all three selected resolution cases along with their fine cases: Test Case 1.

Case	Fine cases		Selected cases	
	nodes	RMSE	nodes	RMSE
Resolution-1	3505403	1.64×10^{-3}	97687	2.43×10^{-3}
Resolution-2	4950405	6.25×10^{-4}	221260	9.85×10^{-4}
Resolution-3	15802299	–	705860	4.80×10^{-4}

Table 4: Validation of point contact results: Test Case 1.

$n_x \times n_y$		Venner [3]		This model			
		H_c	H_m	n_p	Total dof	H_c	H_m
64×64	(=4096)	0.41904	0.28622	4450	10486550	0.42306	0.28921
128×128	(=16384)	0.42872	0.29094	17732	14834838	0.42999	0.29123
256×256	(=65536)	0.43116	0.29218	67350	47440138	0.43129	0.29202

Table 5: A comparison of point contact results over fine and selected meshes: Test Case 1.

n_p	This model (fine-meshes)				This model (selected-meshes)			
	Total dof	H_c	H_m		n_p	Total dof	H_c	H_m
4450	10486550	0.42306	0.28921		1690	294056	0.42242	0.28603
17732	14834838	0.42999	0.29123		4854	666160	0.42842	0.28996
67350	47440138	0.43129	0.29202		16776	2131882	0.43059	0.29167

Table 6: Validation of point contact results: Test Case 2.

		Venner [3]		This model			
$n_x \times n_y$		H_c	H_m	n_p	Total dof	H_c	H_m
64×64	(=4096)	0.070686	0.033080	4450	10486550	0.070251	0.028999
128×128	(=16384)	0.078872	0.037120	17732	14834838	0.078987	0.036286
256×256	(=65536)	0.080935	0.038480	67350	47440138	0.081202	0.038426

Table 7: A comparison of point contact results over fine and selected meshes: Test Case 2.

n_p	This model (fine-meshes)				This model (selected-meshes)			
	Total dof	H_c	H_m		n_p	Total dof	H_c	H_m
4450	10486550	0.070251	0.028999		1690	294056	0.070361	0.027603
17732	14834838	0.078987	0.036286		4854	666160	0.078910	0.035759
67350	47440138	0.081202	0.038426		16776	2131882	0.081243	0.037901

Table 8: Root mean square error of pressure and film thicknesses solutions of various resolution 2 cases with respect to the fine case of resolution 3: Test Case 1.

Case	dof	Pressure RMSE	Film thickness RMSE	t(s)	t/iter	mem.(≈Gb)
Case 1	710906	3.27×10^{-2}	3.10×10^{-3}	1421	203.0	1.6
Case 2	710906	2.71×10^{-2}	3.31×10^{-3}	1397	199.57	1.6
Case 3	670577	2.42×10^{-2}	3.48×10^{-3}	1343	191.86	1.5
Selected case (Res. 2)	666160	2.56×10^{-2}	3.12×10^{-3}	1242	177.43	1.5
Fine case (Res. 2)	14834838	1.39×10^{-2}	1.68×10^{-3}	31681	4525.86	34

Nomenclature

H_0	Central offset film thickness
Ω_c	Contact domain
ϵ	Diffusion coefficient
H_c	Dimensionless central film thickness
$\bar{\rho}$	Dimensionless density
U	Dimensionless displacement vector
H	Dimensionless film thickness
H_m	Dimensionless minimum film thickness
P	Dimensionless pressure
X, Y, Z	Dimensionless space dimensions
λ	Dimensionless speed parameter
$\bar{\eta}$	Dimensionless viscosity
Ω_D	Dirichlet boundary of Ω
D	Elastic deformation
Ω	Elasticity domain
C_{ijkl}	Elasticity tensor
h_e	Element size
ν	Equivalent Poisson ratio
E	Equivalent Young's modulus
V	Fluid velocity field
δ_{ij}	Kronecker delta
λ, μ	Lamé's coefficients
p_h	Maximum Hertzian pressure
M, L	Moes parameters
P^-	Negative pressure
σ_n	Normal stress
n_u	Number of nodes in Ω , excluding Dirichlet boundary nodes
n_p	Number of pressure unknowns
Pe	Peclet number
ξ	Penalty factor
$\mathcal{P}_p, \mathcal{P}_u$	Piecewise linear finite element spaces
u_s	Total speed
Γ_t	Traction boundary of Ω
η_0	Viscosity at ambient pressure
α	Viscosity index
